Nano Research

ISSN 1998-0124 CN 11-5974/O4
https://doi.org/10.26599/NR.2026.94908321

Research Article

Self-powered flexible humidity sensors based on amorphous boron arsenide nanosheets

Zenghui Wu[1], Yuxuan Zhang[1], Boxiang Gao[1], Dongchang He[1], Yan Yan[1], You Meng[1], He Shao[1], Bowen Li[1,2], Weijun Wang[1], Dengji Li[1], Pengshan Xie[1], Dylan Xianyu Fan[3], SenPo Yip[4], Johnny C. Ho[1,2,4,5](✉)

[1] Department of Materials Science and Engineering, City University of Hong Kong, Hong Kong 999077, China

[2] Shenzhen Research Institute, City University of Hong Kong, Shenzhen 518057, China

[3] American International School, Hong Kong 999077, China

[4] Institute for Materials Chemistry and Engineering, Kyushu University, Fukuoka 816-8580, Japan

[5] State Key Laboratory of Terahertz and Millimeter Waves, City University of Hong Kong, Hong Kong 999077, China

Nano Res., **Just Accepted Manuscript** • https://doi.org/10.26599/NR.2026.94908321

https://www.sciopen.com/journal/1998-0124 on Dec. 8, 2025

Just Accepted

TABLE OF CONTENTS (TOC)

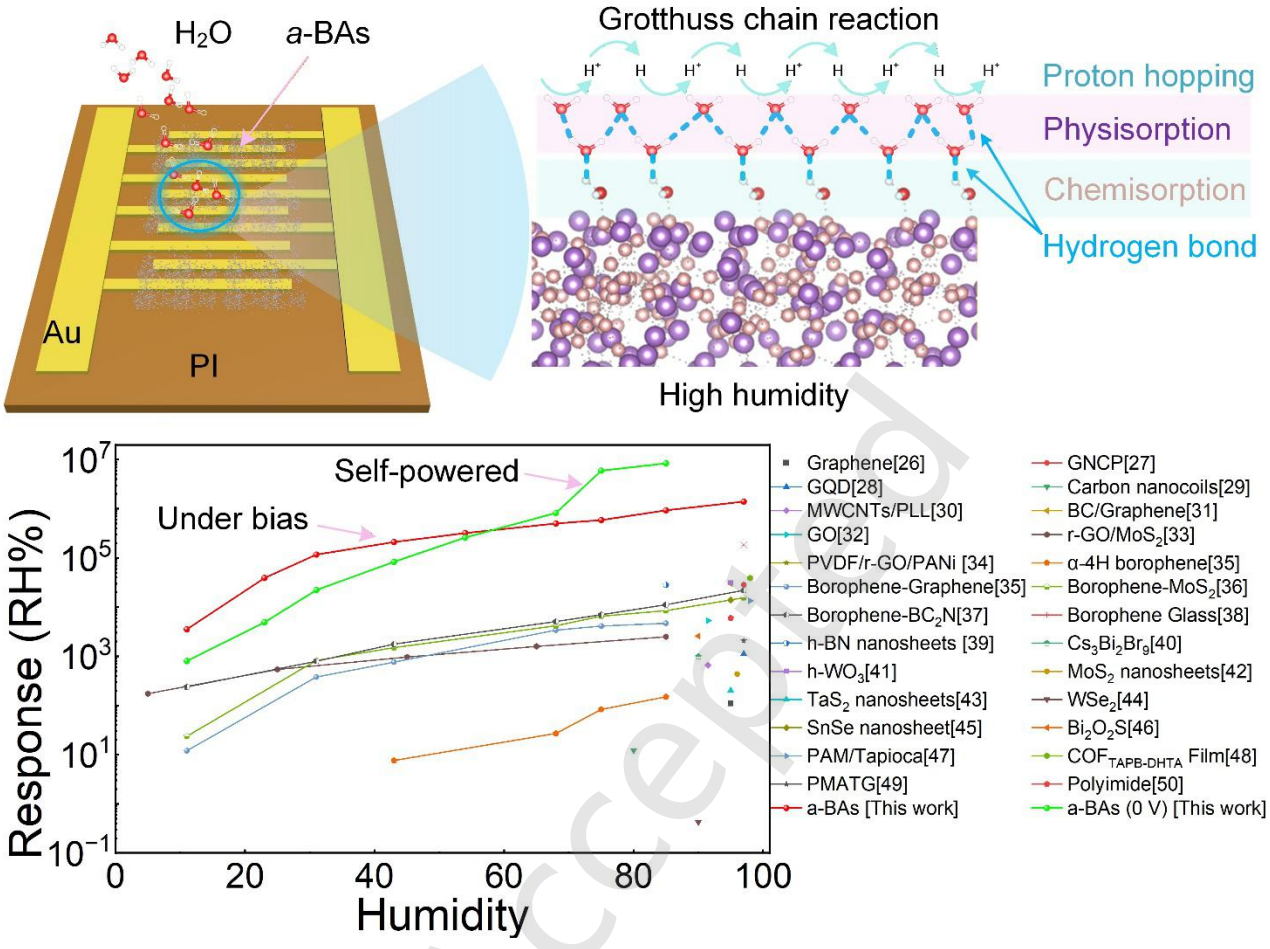

Amorphous boron arsenide (*a*-BAs) nanosheets were synthesised through an innovative in-situ reaction involving elemental arsenic and sodium borohydride within a low-pressure hydrogen-rich environment. The significant influence of water on the electronic conduction of *a*-BAs was revealed, with electronic conduction varying by nearly five orders of magnitude, which paves the way for developing self-powered, high-performance sensing materials.

Nano Research

Open Access

Research Article

Self-powered flexible humidity sensors based on amorphous boron arsenide nanosheets

Zenghui Wu[1], Yuxuan Zhang[1], Boxiang Gao[1], Dongchang He[1], Yan Yan[1], You Meng[1], He Shao[1], Bowen Li[1,2], Weijun Wang[1], Dengji Li[1], Pengshan Xie[1], Dylan Xianyu Fan[3], SenPo Yip[4], and Johnny C. Ho[1,2,4,5] ✉

[1] *Department of Materials Science and Engineering, City University of Hong Kong, Hong Kong 999077, China*
[2] *Shenzhen Research Institute, City University of Hong Kong, Shenzhen 518057, China*
[3] *American International School, Hong Kong 999077, China*
[4] *Institute for Materials Chemistry and Engineering, Kyushu University, Fukuoka 816-8580, Japan*
[5] *State Key Laboratory of Terahertz and Millimeter Waves, City University of Hong Kong, Hong Kong 999077, China*

Received: 27 September 2025; **Revised:** 2 December 2025; **Accepted:** 8 December 2025

✉ Address correspondence to johnnyho@cityu.edu.hk

Cite this article: *Nano Research*, **2026**, *19*, 94908321. https://doi.org/10.26599/NR.2026.94908321

ABSTRACT: Boron arsenide, renowned for its ambipolar charge mobility and superior thermal conductivity, has emerged as a focal point of contemporary research. Despite its promising properties, the impact of water on the electronic conductivity (EC) of boron arsenide remains largely unexplored. In this study, we synthesized amorphous boron arsenide (*a*-BAs) nanosheets through an innovative in situ reaction involving elemental arsenic and sodium borohydride within a low-pressure, hydrogen-rich environment. We performed both theoretical and experimental analyses to investigate the influence of water on EC in representative *a*-BAs. These nanosheets were integrated into self-powered, flexible humidity sensors, demonstrating a substantial current change across nearly five orders of magnitude and achieving an extraordinary response of 8.4 × 10^6% at 85% RH without an additional power unit. The sensors exhibited a remarkable linear correlation between the logarithmic response function and a wide-ranging detection capability (11-97% RH), achieving an extraordinary response of 1.4 × 10^6% at 97% RH under a 1 V bias. This research not only introduces a straightforward synthesis method for amorphous boron arsenide nanosheets but also highlights the significant impact of water on the EC of boron arsenide, paving the way for developing self-powered high-performance sensing materials.

KEYWORDS: boron arsenide, humidity sensor, amorphous, noncontact sensing

1 Introduction

Accurate monitoring of environmental humidity is crucial across various fields, including aerospace, agriculture, industrial production, environmental protection, and human healthcare, which impact living comfort [1-3]. Consequently, humidity sensors have become one of the most extensively researched and utilized chemical sensors, focusing on maximizing device performance through component optimization and refining operational mechanisms [3-5]. In recent decades, a growing demand for zero-power consumption and flexible humidity detection has been driven by emerging self-powered flexible materials technologies [6, 7]. Among various moisture-sensitive systems, nanomaterials, especially two-dimensional (2D) materials, are excellent candidates for humidity sensing applications because of their large specific surface area, numerous active sites, adjustable electro-mechanical characteristics, and exceptional environmental sensitivity [8-12]. However, most 2D materials-based humidity sensors exhibit linear responses over a narrow relative humidity (RH) range, with response changes spanning one or two orders of magnitude [13-15]. Thus, developing novel materials with enhanced hydrophilicity and superior charge transport capabilities remains a significant challenge for achieving robust and efficient water molecule detection.

Boron arsenide (BAs), a relatively unexplored III-V semiconductor due to difficulties in its synthesis, has recently attracted considerable research attention. This surge is driven by its extraordinary properties, such as ultrahigh thermal conductivity (1300 W/mK) and distinctive carrier mobility (hole: 2110 cm^2/Vs; electron: 1400 cm^2/Vs), validated by both theoretical predictions and experimental synthesis [16-23]. However, research on amorphous boron arsenide nanosheets remains at the stage of theoretical computation [24-26]. Although numerous amorphous and boron-based materials are known to adsorb substantial amounts of water even at low RH levels [9, 10, 27-29], the

synthesis of amorphous boron arsenide has been infrequently reported, and the impact of water on its electronic conductivity and potential device applications remains unmapped.

In this study, we successfully synthesized amorphous boron arsenide nanosheets (*a*-BAsNSs) for the first time via in situ heating a mixture of $NaBH_4$ and arsenic within a hydrogen-rich atmosphere. We investigated the influence of water on the electronic conduction of *a*-BAs, revealing an unexpectedly large modulation, with electronic conduction varying by up to nearly five orders of magnitude. The underlying mechanism was elucidated through a combination of experimental and theoretical analyses. Furthermore, a self-powered high-performance humidity sensor was developed, leveraging the significant impact of water on the conductivity of a-BAs. Compared to existing 2D materials used in humidity sensing, our sensor achieves unprecedented sensitivity, a broad detection range, high selectivity, and excellent long-term stability, while exhibiting convenient, low-cost, and low-power consumption manufacturing.

2 Results and discussion

2.1. Preparation and characterization of the a-BAsNS

Fig. 1a provides a graphical summary of the synthesis process for *a*-BAsNSs. A standardized thermal processing methodology was established to fabricate large-area, freesta-

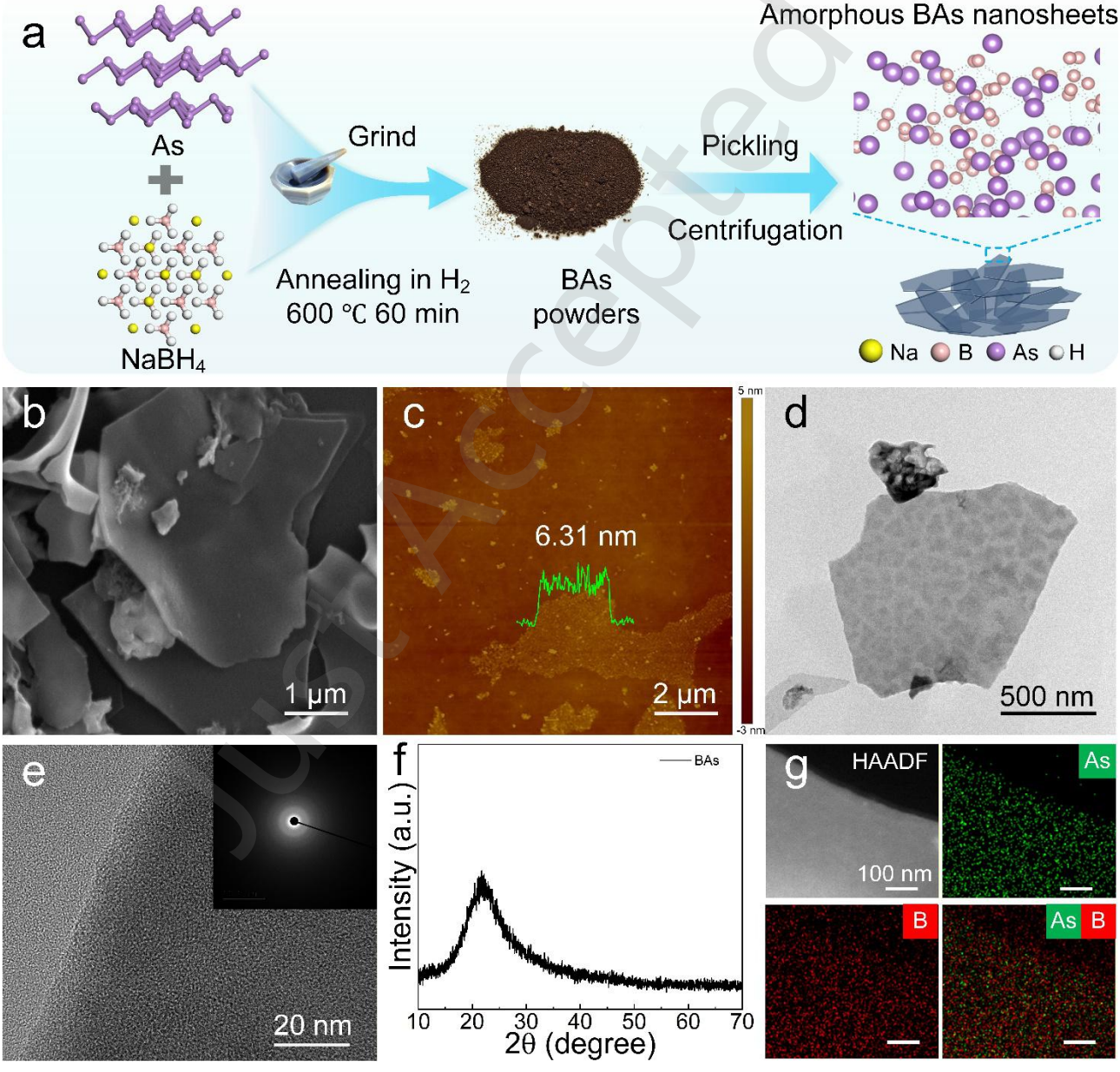

Figure 1 Diagrammatic synthesis process and morphological analysis of the *a*-BAsNSs. (a) Diagrammatic synthesis process of *a*-BAsNS. (b) SEM image of *a*-BAsNSs. (c) AFM image of the *a*-BAsNSs. (d) Low-magnification TEM image of a typical *a*-BAsNS. (e) High-magnification TEM image of the *a*-BAsNSs. The inset in the top right corner is the corresponding SAED pattern image of the *a*-BAsNSs. (f) XRD of the *a*-BAsNSs. (g) HAADF-STEM-EDS elemental mappings of a typical *a*-BAsNSs.

nding boron arsenide through the in-situ decomposition of $NaBH_4$ precursors and arsenic incorporation. The precursor

mixture underwent a controlled thermal ramp from ambient conditions to 600 °C (Fig. S1 in the Electronic Supplementary Material (ESM)), with subsequent isothermal maintenance at the target temperature for 60 minutes to obtain *a*-BAsNSs. A comprehensive explanation of the synthesis procedure will be systematically presented in the Experimental Section (see the Experimental Section in the Electronic Supplementary Material, ESM). Post-synthesis processing involved sequential centrifugal separation and purification steps to prepare analytical-grade specimens for subsequent material characterization. Fig. 1b presents the scanning electron microscopy (SEM) images of the *a*-BAsNSs, highlighting their irregular structural morphology. The thickness and lateral size of the sheets were further characterized via atomic force microscopy (AFM) (Fig. 1c), revealing a characteristic thickness of 6.31 nm with lateral extensions spanning several micrometers. These dimensional parameters were corroborated by low-magnification transmission electron microscopy (LRTEM) observations (Fig. 1d), which confirmed the thin morphology and structural irregularity matching AFM measurements (Fig. 1c). Crystallographic evaluation through high-resolution transmission electron microscopy (HRTEM) imaging (Fig. 1d) and selected-area electron diffraction (SAED) patterns from representative zones (Fig. 1e) revealed the complete absence of lattice periodicity, confirming the amorphous phase constitution. This non-crystalline nature was further confirmed by X-ray diffraction (XRD) analysis (Fig. 1f), exhibiting no perceptible crystalline domains or long-range order. Additionally, energy-dispersive X-ray spectroscopy (EDS) mapping was employed to verify the chemical composition of the synthesized *a*-BAsNS. The analysis revealed an elemental ratio of boron to arsenic of approximately 1:1, along with uniform elemental distribution (Fig. S2 in the ESM). This confirms the successful controlled synthesis of compositionally uniform *a*-BAsNSs.

2.2. Chemical state and optical properties of *a*-BAsNS

To investigate the surface composition and chemical state of the *a*-BAsNS, X-ray photoelectron spectroscopy (XPS) was systematically analyzed, as shown in Fig. 2. Spectral calibration was performed using the adventitious carbon C 1s peak referenced to 284.8 eV (Fig. 2b), ensuring binding energy accuracy for subsequent elemental analysis. The high-resolution B1s signal can be deconvoluted into two peaks at 187.7 and 188.8 eV (Fig. 2c), which are in the range reported for boride [30, 31]. The As 3d spectrum (Fig. 2d) displayed peaks at 41.4 eV ($3d_{5/2}$) and 42.8 eV ($3d_{3/2}$), consistent with arsenic in bonding configurations characteristic of boron arsenide phases in the range reported for boron arsenides [30, 31].

Raman spectroscopic analysis was conducted to probe the structural and vibrational characteristics of the *a*-BAsNSs, revealing distinct phononic signatures absent in precursor materials (Fig. 2e). The spectrum exhibits two broad vibrational modes centered at 228.2 cm^{-1} (150.2–313.9 cm^{-1}) and 815.7 cm^{-1} (737.8–903.5 cm^{-1}), characteristic of amorphous B-As bonding configurations. These features starkly contrast with the sharp phonon modes observed in the raw precursor mixture (Fig. S3a in the ESM), confirming the structural reorganization induced by the synthesis protocol. Attenuated total reflectance Fourier-transform infrared (ATR-FTIR) spectra further corroborated the unique bonding environment of *a*-BAsNSs (Fig. 2f). Three broad absorption bands centered at 632, 817, and 1441 cm^{-1} were resolved, absent in the precursor spectra (Fig. S3b in the ESM). These bands correspond to B-As stretching vibrations and out-of-pl-

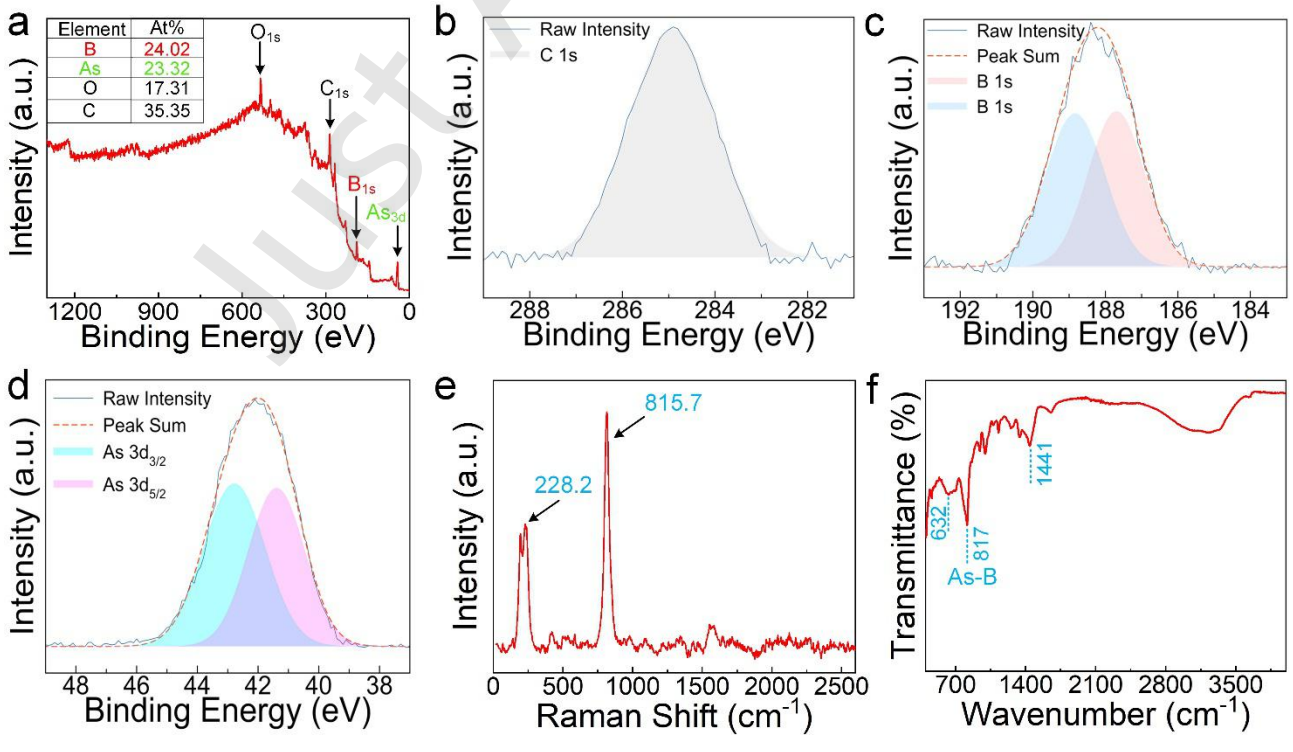

Figure 2 Chemical state and optical properties of *a*-BAsNS. (a) Full-scale XPS survey of the *a*-BAsNS. (b-d) High-resolution spectra of C 1s, B 1s, and As 3d of the *a*-BAsNS. (e) Raman and (f) ATR-FTIR spectra of the *a*-BAsNS.

ane deformations, consistent with forming a disordered covalent network lacking long-range periodicity. The combined Raman and ATR-FTIR analyses demonstrate a complete transformation from precursor-derived crystalline phases to an amorphous boron arsenide system, with spectral broadening indicative of structural disorder and phonon confinement effects.

2.3. Self-powered flexible a-BAsNSs humidity sensor

To evaluate the technological viability of *a*-BAsNSs in next-generation electronics, we engineered a flexible humidity sensor architecture using ultrathin polyimide (PI) substrates. The device and sketch of the experimental setup with static saturated salt solutions are shown in **Fig. 3**a. The test details are provided in the Experimental section (see Electronic Supplementary Material, ESM). This platform enabled systematic investigation of humidity-responsive electrical behavior through real-time current monitoring across a comprehensive relative gradient (0–97%)

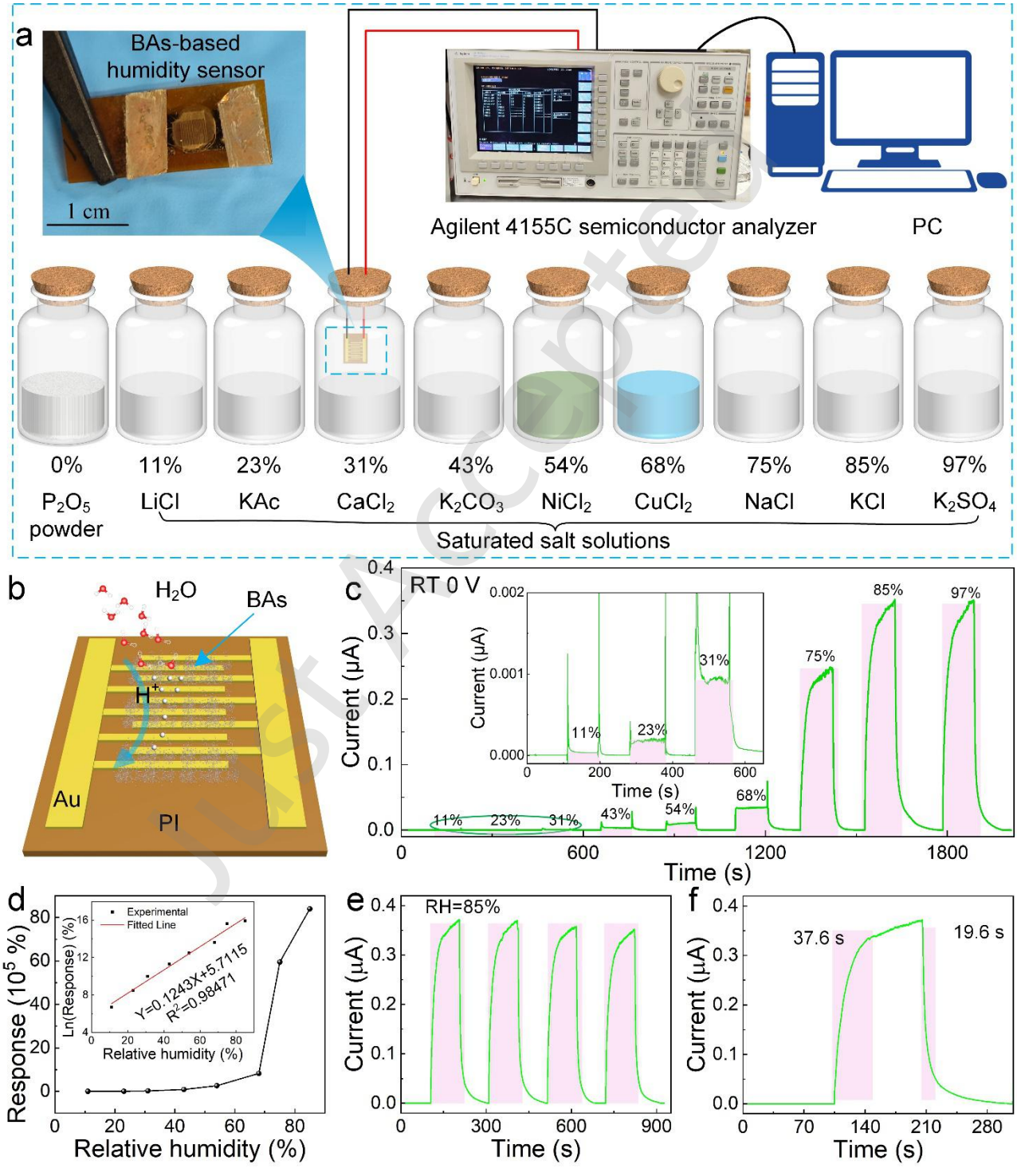

Figure 3 Sketch of the experimental setup for the humidity test and characterization of the *a*-BAs humidity sensor under 0 V bias. (a) The device and a sketch of the experimental setup for the humidity test. (b) Schematic ion diffusion mechanism of the humidity sensor under 0 V bias. (c) Real-time

response of the sensor during RH switching. (d) Response of the sensor across the range of 11% to 85% RH. (e) Cycle stability of the sensor at 85% RH. (f) Response and recovery curve of the sensor at 85% RH.

at 0 V bias. As shown in Fig. S4 in the ESM, the output voltage and current of the device can be maintained for more than 1 h without significant attenuation at 85% RH at room temperature. The underlying working mechanism of the *a*-BasNSs-based moist-electric humidity sensor is fundamentally governed by a process of ion diffusion, which facilitates moisture-enabled electricity generation [2], as exhibited in Fig. 3b. A desiccative P_2O_5 environment (0% RH) served as the baseline for signal normalization [9, 10, 27].

Controlled RH conditions were established via equilibrium vapor pressure in sealed chambers containing different saturated salt solutions: LiCl (11%), KAc (23%), $CaCl_2$ (31%), K_2CO_3 (43%), $NiCl_2$ (54%), $CuCl_2$ (68%), NaCl (75%), KCl (85%), and K_2SO_4 (97%), consistent with established hygrometric protocols. Sensor response (R) was quantified using the relationship:

$$R\,(\%) = (I_{RH}\text{-}I_0)/I_0 \times 100\% \quad (1)$$

where I_{RH} and I_0 denote the sensor's current in a given RH and dry air, respectively [10, 28]. During the experiments, the sensor was rapidly transitioned between the dry environment and the target humidity level, where it was then held for approximately 120 s in the dry or moist atmosphere.

The dynamic current response of the humidity-sensing device was systematically recorded under RH variations spanning 0-97% (Fig. 3c). Notably, the fabricated material exhibited a pronounced current modulation from 4.15 pA under anhydrous conditions (0% RH) to 0.35 μA at high moisture levels (85% RH), demonstrating a near five orders of magnitude response enhancement. It is worth noting that the response current at a relative humidity of 97% is almost the same as that at a relative humidity of 85%, indicating that the device is saturated at a relative humidity of 85%. Through the systematic signal transformation of the raw data (Fig. 3c), we established the quantitative correlation between sensor response and relative moisture levels (Fig. 3d), which can be fitted with the formula: Y = 0.1243X +5.7115 (R^2 = 0.98471), as shown in the inset of Fig. 3d. The findings indicate that post-processing of data enables precise determination of rela-

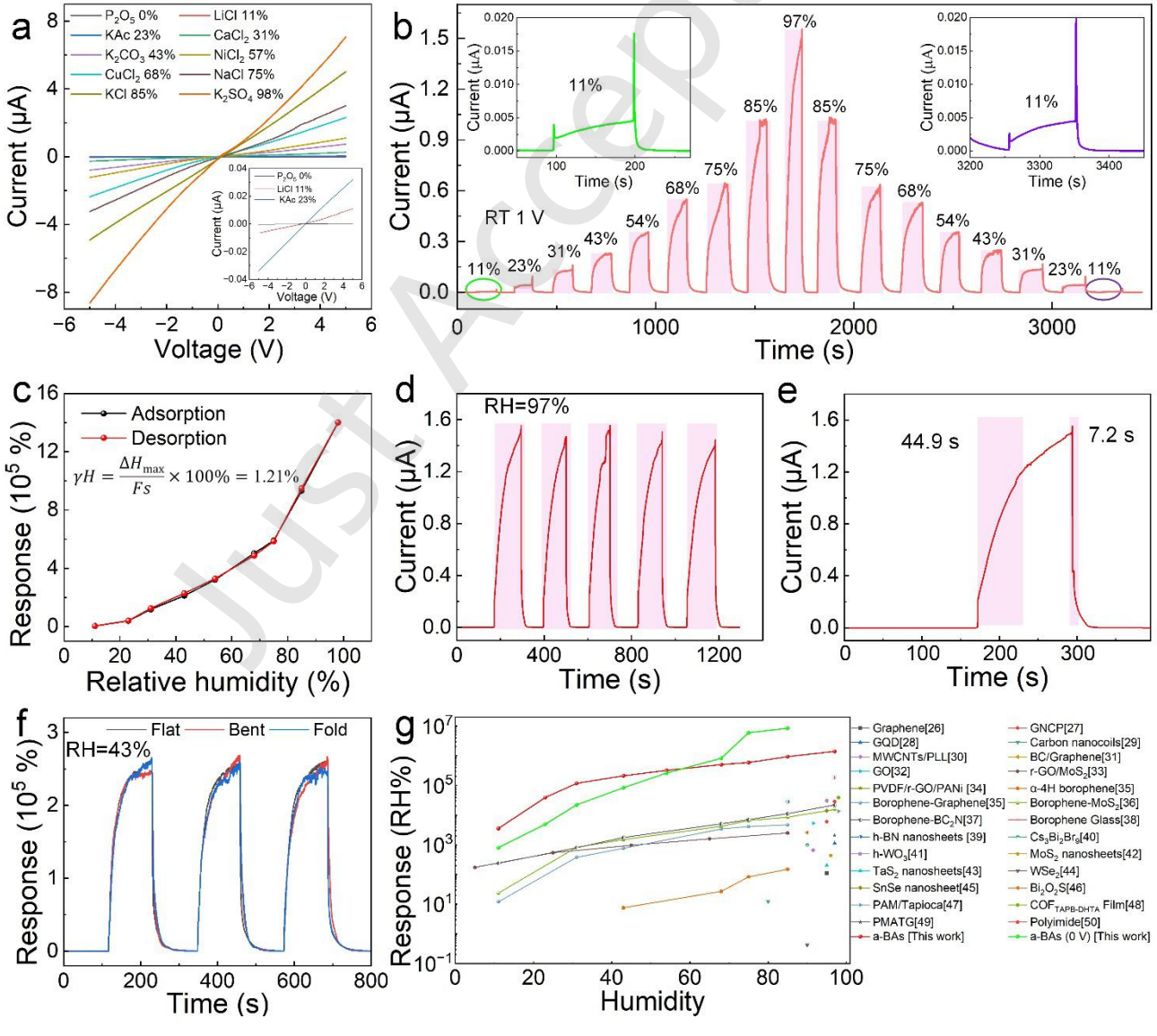

Figure 4 Characterization of the *a*-BAs humidity sensor under bias. (a) I–V characteristics of the BAs-based humidity sensor in an ambient environment with different RH under 5 V bias. (b) Real-time response of the sensor under switching RH. (c) Hysteresis curve of the sensor in the range of 11% to 97% RH. (d) Cycle stability of the sensor at 97% RH. (e) Response and recovery curve of the sensor at 97% RH. (f) Response curves of the sensor under bent and flat states at 43% RH. (g) Comparison with other recent works on optimal response.

tive humidity from the initial measurements. Notably, the optimized architecture achieved a record humidity response of 8.4 × 10^6% at 85% RH. The cyclic stability assessment of *a*-BAsNSs-based hygrometers under 85% RH conditions (Fig. 3e) demonstrated reproducible switching behavior. To validate operational robustness across environmentally relevant humidity gradients, seven distinct RH benchmarks (11-75% RH) were subjected to iterative testing protocols (Fig. S5 in the ESM). Statistical analysis revealed negligible degradation in responsivity throughout several continuous operations, confirming multicycle environmental tolerance. In addition, transient response kinetics characterization of the *a*-BAsNSs sensor (Fig. 3f) recorded response/recovery times of 37.6 and 19.6 s, respectively, at 85% RH, which are defined as the time required for 90% of the total change in current, and this performance is superior to many commercial humidity sensors. This indicates that the time required for water molecules to reach saturation upon adsorption on the boron arsenide surface is longer than the time needed for desorption to occur.

Furthermore, we conducted a similar investigation of humidity-responsive electrical behavior across a comprehensive relative humidity (RH) gradient (0–97%) at 1 V bias. The representative I–V characteristics of the BAs-based humidity sensor in an ambient environment with different RH within a potential window of −5 to +5 V (Fig. 4a). The curves exhibit a consistent trend demonstrating that the current increases with rising relative humidity (RH), which suggests that adsorbed H_2O molecules act as electron acceptors, leading to a conductivity variation. The dynamic current response of the humidity-sensing device was systematically recorded across cyclic RH variations spanning 0-97% under 1 V bias (Fig. 4b). Notably, the fabricated material exhibited a pronounced current modulation from 34 pA under anhydrous conditions (0% RH) to 1.55 μA at near-saturation moisture levels (97% RH), demonstrating four orders of magnitude response enhancement. Through the systematic signal transformation of the raw data (Fig. 4b), we established the quantitative correlation between sensor response and ambient moisture levels (Fig. S6 in the ESM). The results show that relative humidity measurement can be accurately realized via the corresponding relative humidity after data processing over a wide range of values. To examine the humidity hysteresis behavior of the sensor, Fig. S7 in the ESM presents the current curves during the adsorption and desorption phases of water molecules. These curves illustrate the sensor's excellent step response and recovery capabilities. Hysteresis analysis across the critical 11-97% RH operational range (Fig. 4c) yielded a remarkably low hysteresis coefficient of 1.21%. This minimal path dependence conclusively demonstrates that the sensor's electrical output constitutes a state function determined solely by instantaneous RH values, independent of temporal humidity gradients. The observed performance metrics position this technology for precision environmental monitoring and industrial process control applications. The cyclic stability assessment of *a*-BASNSs-based hygrometers under 97% RH saturation conditions (Fig. 4d) demonstrated reproducible switching behavior. To validate operational robustness across environmentally relevant humidity gradients, eight distinct RH benchmarks (11-85% RH) were subjected to iterative testing protocols (Fig. S8 in the ESM). Statistical analysis revealed negligible degradation in responsivity throughout several continuous operations, confirming multicycle environmental tolerance.

In addition, transient response kinetics characterization of the *a*-BAsNSs sensor at 97% RH, recorded response/recovery times of 44.9 and 7.2 s, respectively (Fig. 4e). The sensor's response curves exhibit no significant alterations after being exposed to ambient conditions for four weeks, demonstrating its suitability for long-term practical use (Fig. S9 in the ESM). For flexible electronics integration validation, multiaxial strain tolerance tests were conducted under controlled deformation modes: (i) planar, (ii) bent, and (iii) folded configurations. As illustrated in Fig. 4f, the sensor operates effectively in any condition at 43% RH, with its associated response remaining nearly constant. The findings indicate that the a-BAsNS sensor exhibits excellent stability and mechanical flexibility. Significantly, the optimized design attained an unprecedented humidity response of 1.4 × 10^6% at 97% RH. The performance of a-BAsNS sensors was evaluated against the most recent resistive humidity sensors made from conventional materials (Fig. 4g and Table S1 in the ESM). These materials comprised h-BN nanosheets (2.8 × 10^4%) [32], perovskites ($Cs_3Bi_2Br_9$, 987%) [33], metal oxides (*h*-WO_3, 3.1 × 10^4%) [6], carbon-based low-dimensional materials [34-38], like graphene (110%) [39], graphene quantum dots (GQDs, 1.1 × 10^3%) [40], graphene oxide (GO, 5.3 × 10^3%) [41], multi-walled carbon nanotubes (MWCNTs, 659.97%) [42], transition metal chalcogenides [13, 14], like MoS_2 nanosheets (434%) [15], TaS_2 nanosheets (201.9%) [43], SnSe nanosheets (1.4 × 10^4%) [44], boron-based materials, like borophene (150%) [27], borophene glass (1.8 × 10^5%) [28], borophene-based heterostructure [9, 10, 27], organic material [45, 46], like COF (3.9 × 10^4%) [47], and Polyimide (6.0 × 10^3%) [48]. Notably, the *a*-BasNSs-based humidity sensor demonstrated the highest response compared to all the resistive humidity sensors documented in these works.

2.4. Moisture-sensitive mechanism of a-BAsNSs

The fundamental understanding of the water-solid interface is pivotal for elucidating the unique humidity-responsive behavior of *a*-BAsNSs (Fig. 5). The surface chemistry and structural characteristics of these materials can significantly influence the kinetics of water molecule adsorption/desorption processes, which in turn underpin their exceptional sensing performance. Specifically, the sensor exhibits superior characteristics, characterized by rapid response kinetics and exceptional response, largely

due to the Grotthuss mechanism that governs proton transfer dynamics at the interface [49, 50]. The humidity sensing mechanism operates through the chemisorption and subsequent physical adsorption of H_2O molecules on the *a*-BAsNSs surface, where protons serve as effective charge carriers. Initially, chemisorbed H_2O layers are formed at lower RH levels. A minor portion of H_2O molecules adsorb on the *a*- BAsNSs surface and subsequently dissociate ($H_2O \rightarrow H^+ + OH^-$), forming a barrier layer (Fig. 5d) [49]. This barrier layer restricts the mobility of water molecules. The OH^- ions are identified as electron donors that can be readily absorbed in

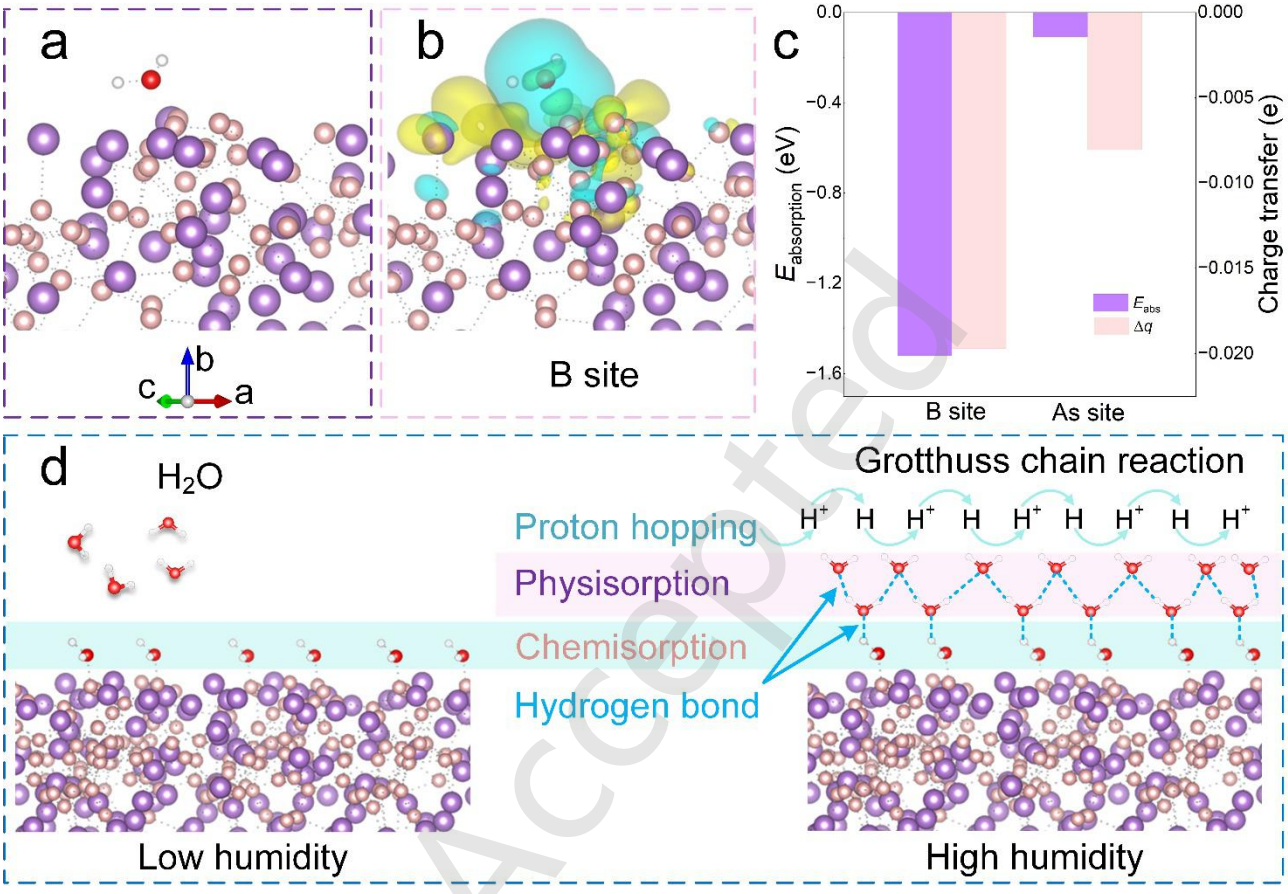

Figure 5 Theoretical elucidation of *a*-BAs humidity sensing mechanism. (a) Side views of the *a*-BAs structures with the H_2O molecule. (b) Charge density difference of the *a*-BAs with the H_2O molecule. (c) Evaluation of adsorption energies and charge transfer across various adsorption sites. (d) A schematic representation illustrating the humidity sensing mechanism of the a-BAs sensor under different humidity levels.

boron sites on the surface of BAs nanosheets, thereby facilitating the generation of additional free protons, H^+, and enhancing the material's conductivity. As RH increases, additional H_2O molecules undergo physical adsorption onto the chemisorbed layer, progressively enhancing the sensor's response. From the second physically adsorbed layer, H_2O molecules are physisorbed via single hydrogen bonding to hydroxyl groups. Consequently, the sensor exhibits an electrically linear response within the low-to-moderate RH range (11–75% RH), with a relatively small current variation consistent with experimental results (as demonstrated in Fig. 4a and Fig. 5a). As physical adsorption progresses, the multilayer structure of H_2O molecules continues to grow. At higher humidity levels, generating hydronium ions (H_3O^+) as charge carriers facilitates the electrostatic field-induced dissociation of water molecules. This process is accompanied by a progressive adsorption behavior where monolayer and multilayer physisorption transitions occur. The associated proton transport mechanism involves an ionic conduction pathway, characterized by the Grotthuss chain reaction ($H_2O + H_3O^+ \leftrightarrow H_3O^+ + H_2O$), which promotes charge propagation through the material matrix [14, 49]. Notably, the dissociated H_3O^+ ions act as effective hole acceptors within the *a*-BAs nanosheets, significantly enhancing their electrical conductivity. With an increase in relative humidity from 75% to 97%, the gradient of the linear relationship becomes more pronounced, leading to a significant change in current (Fig. 4c and Fig. S6 in the ESM). At high humidity levels, free water molecules penetrate the *a*-BAsNSs, creating favorable conditions for enhanced sensor performance. This interpenetration facilitates a marked improvement in both sensitivity and response characteristics. The material exhibits two distinct conductive states directly correlated with varying RH levels, resulting in pronounced changes in its electrical properties. These findings provide a comprehensive understanding of the humidity-dependent conductivity mechanism in *a*-BAs.

Furthermore, first-principles density functional theory (DFT) calculations were conducted to systematically investigate the adsorption characteristics of H_2O molecules on *a*-BAs (see the Experimental section in the ESM). The investigation focused on two specific adsorption sites: B and

As surface sites (Fig. 5a). Through geometric optimizations, the configurations of adsorbed H_2O molecules that exhibit the greatest stability at these sites were determined (Fig. 5b). Adsorption energies (E_{ads}) were determined using the following thermodynamic relation:

$$E_{ads} = E_{a\text{-BAs-}H_2O} - E_{H_2O} - E_{a\text{-BAs}} \quad (2)$$

where $E_{a\text{-BAs-}H_2O}$ denotes the total energy of H_2O when adsorbed onto *a*-BAs, E_{H_2O} refers to the energy of the H_2O molecule in its gaseous state, and $E_{a\text{-BAs}}$ corresponds to the energy of *a*-BAs itself [28]. Fig. 5c illustrates the computed adsorption energy (E_{ads}) and Bader charge transfer ($\triangle$q) for the two adsorption sites. A positive $\triangle$q signifies hole doping, whereas a negative $\triangle$ q indicates electron doping. The results suggest that the B site of *a*-BAs is the most favorable adsorption configuration, with a maximum E_{ads} of -1.52 eV, indicating a relatively strong interaction between *a*-BAs and water molecules. Bader charge analysis reveals that water molecules acquire 0.02 e from *a*-BAs. Furthermore, the E_{ads} and $\triangle$ q values at the B site surpass those at the As site, indicating that reduced hydrogen passivation might be more advantageous for humidity sensing. In addition, the charge density difference (CDD) visualization offers a comprehensive quantification of charge transfer, thereby clarifying the interaction between a-BAs and water molecules (Fig. 4b). The CDD image is derived using the following equation:

$$\Delta\rho = \rho_{BAs\text{-}H_2O} - \rho_{H_2O} - \rho_{BAs} \quad (5)$$

where $\rho_{BAs\text{-}H_2O}$, ρ_{H_2O} and ρ_{BAs} denote the total charge density of H_2O/*a*-BAs system, the isolated H_2O molecule, and the pristine *a*-BAs, respectively. The adsorption of H_2O molecules leads to pronounced modifications in *a*-BAs's charge distribution. The oxygen atom in H_2O is mainly associated with a blue region. In contrast, the neighboring *a*-BAs are characterized by a yellow region, indicating substantial charge transfer from the *a*-BAs lattice to the adsorbed water molecules. This highlights the specifics of water adsorption on a-BAs nanosheets under low-humidity conditions, providing insights into the underlying mechanisms of humidity sensing at reduced dimensions.

3. Conclusion

In conclusion, we have successfully fabricated amorphous BAs nanosheets via a controlled in situ thermal decomposition route, and their implementation as a self-powered, flexible, and moisture-sensitive humidity sensor. The resulting *a*-BAs-based sensor exhibits an extraordinary response of 8.4 × 10^6% at 85% RH without requiring an additional power unit. Notably, the sensor achieves a wide sensing range (11–97% RH), minimal hysteresis, outstanding reproducibility, and exceptional long-term stability, as well as an exceptional response of 1.4 × 10^6% at 97% RH under a 1 V bias, surpassing all previously reported 2D material-based sensors. DFT calculations provide mechanistic insights, attributing the sensing capability to the charge transfer dynamics facilitated by adsorbed water molecules. Furthermore, the device exhibits excellent mechanical flexibility. These findings establish *a*-BAs as a promising material platform for advanced humidity sensing technologies with the potential for practical applications.

Electronic Supplementary Material: Supplementary material (The experimental sections, additional Raman, IR spectrum data of the sources, and additional data of the performance of the humidity sensor) is available in the online version of this article at https://doi.org/10.26599/NR.2026.94908321.

Data availability

All data needed to support the conclusions in the paper are presented in the manuscript and the Electronic Supplementary Material. Additional data related to this paper may be requested from the corresponding author upon request.

Acknowledgements

This work is supported by a fellowship award from the Research Grants Council of the Hong Kong Special Administrative Region, China (CityURFS2021-1S04), the Innovation and Technology Fund (MHP/044/23) from the Innovation and Technology Commission of the Hong Kong Special Administrative Region, China, the Science Technology and Innovation Committee of Shenzhen Municipality (Project No. JCYJ20230807114910021), and Guangdong Basic and Applied Basic Research Fund (Project no. 2024A1515011922).

Declaration of competing interest

All the contributing authors report no conflicts of interest in this work.

Author contribution statement

Z.H.W. and J.C.H. conceived and initiated the project. Z.H.W. prepared materials, fabricated devices, and performed analysis. Y.X.Z. and D.C.H. performed the DFT calculation. B.X.G. contributed to the XPS test. Y.Y. and Y.X.Z. conducted the AFM measurements. Y.M., H.S., B.W.L., W.J.W., D.J.L., P.S.X., D.X.Y.F., and S. P. Y. helped with the electrical measurement. Z.H.W. and J.C.H. wrote the initial manuscript. All authors contributed to the final manuscript and approved the submission.

Use of AI statement

None.

References

[1] Yin, R. Y.; Wang, D. P.; Zhao, S. F.; Lou, Z.; Shen, G. Z., Wearable sensors-enabled human-machine interaction systems: from design to application. *Adv. Funct. Mater.* **2021**, *31* (11), 2008936.

[2] Tan, J.; Wang, X.; Chu, W. C.; Fang, S. M.; Zheng, C. X.; Xue, M. M.; Wang, X. F.; Hu, T.; Guo, W. L., Harvesting energy from atmospheric water: grand challenges in continuous electricity generation. *Adv. Mater.* **2024**, *36* (12), 2211165.

[3] Montes-Garcia, V.; Samori, P., Humidity sensing with supramolecular nanostructures. *Adv. Mater.*, **2024**, *36* (12), 2208766.

[4] Liao, K.X., Wang, F.J., Shen, Q.R., Liu, Y.F., Mei, Z.X., Wang, H., Zhang, S.Z., Ma, S.F., Wang, L.Q., Advances in humidity sensors based on self-powered technology, *Chem. Eng. J*, **2025**, *505*, 159480.

[5] Duan, Z.H., Jiang, Y.D., Tai, H.L., Recent advances in humidity

sensors for human body related humidity detection, *J Mater. Chem. C*, **2021**, *9*, 14963-14980.

[6] Guo, P. W.; Tian, B.; Liang, J.; Yang, X. P.; Tang, G. L.; Li, Q. C.; Liu, Q.; Zheng, K.; Chen, X.; Wu, W., An all-printed, fast-response flexible humidity sensor based on hexagonal-WO_3 nanowires for multifunctional applications. *Adv. Mater.* **2023**, *35* (41), 2304420.

[7] Zhang, M. X., Duan, Z. H., Yuan, Z., Jiang, Y.D., Tai, Y. L. Observing mixed chemical reactions at the positive electrode in the high-performance self-powered electrochemical humidity sensor, *ACS Nano*, 2024, 18, 34158-34170.

[8] Chen, L. M.; Hu, K.; Lu, M. Y.; Chen, Z. Q.; Chen, X. W.; Zhou, T. Q.; Liu, X. Q.; Yin, W. L.; Casiraghi, C.; Song, X. J., Wearable sensors for breath monitoring based on water-based hexagonal boron nitride inks made with supramolecular functionalization. *Adv. Mater.* **2024**, *36* (18), 2312621.

[9] Hou, C.; Tai, G. A.; Liu, Y.; Wu, Z. T.; Wu, Z. H.; Liang, X. C., Ultrasensitive humidity sensing and the multifunctional applications of borophene-MoS_2 heterostructures. *J Mater. Chem. A* **2021**, *9* (22), 13100-13108.

[10] Liu, X.; Hou, C.; Liu, Y.; Chen, S. F.; Wu, Z. T.; Liang, X. C.; Tai, G. A., Borophene and BC_2N quantum dot heterostructures: ultrasensitive humidity sensing and multifunctional applications. *J Mater. Chem. A* **2023**, *11* (45), 24789-24799.

[11] Alam, Abid, N., Islam, S.S., Advancements in trace and low humidity sensors technologies using nanomaterials: A review, *ACS Appl. Nano Mater.*, **2024**, 7, 13836-13864.

[12] Rehman, M.M., Khan, M. Rehman, H.M.M.u. Siddiqui, G.U., Ahmad, Z., Ali, K., Khan, S.A., Saqib, Gul, M. J., Kim, W.Y., Chapter 20 - nanomaterials in humidity sensors, in: Malik, M.I., Hussain, D., Shah, M.R., Guo, D.-S. (Eds.) *Handbook of nanomaterials*, volume 1, *Elsevier* 2024, 513-566.

[13] Bhadra, J.; Sassi, L. M.; Oliveira, E. F.; Hachtel, J. A.; Parangusan, H.; Mallick, S. A.; Ahmad, Z.; Galvao, D. S.; Puthirath, A. B.; Vajtai, R.; Ajayan, P. M.; Al-Thani, N., An impedance humidity sensor based on CVD grown WSe_2 2D films. *ACS Appl. Electron. Mater.* **2024**, *6* (11), 7734-7743.

[14] Wei, C. D.; Zhu, M.; Zhou, Z. Z.; Zhao, S.; Mao, J. P.; Yin, D. M.; Li, J. Y.; Wang, Y.; Hao, J. Y., Two-dimensional Bi_2O_2S based high-sensitivity and rapid-response humidity sensor for respiratory monitoring and Human-Machine Interaction. *Chem. Eng. J.* **2024**, 485, 149805.

[15] Siddiqui, M. S.; Mandal, A.; Kalita, H.; Aslam, M., Highly sensitive few-layer MoS_2 nanosheets as a stable soil moisture and humidity sensor. *Sensors and Actuat. B-Chem.* **2022**, 365.

[16] Kang, J. S.; Li, M.; Wu, H. A.; Nguyen, H.; Hu, Y. J., Experimental observation of high thermal conductivity in boron arsenide. *Science*, **2022**, *361* (6402), 575-578.

[17] Li, S.; Zheng, Q. Y.; Lv, Y. C.; Liu, X. Y.; Wang, X. Q.; Huang, P. S. E. Y.; Cahill, D. G.; Lv, B., High thermal conductivity in cubic boron arsenide crystals. *Science*, **2018**, *361* (6402), 579-581.

[18] Yue, S.; Tian, F.; Sui, X. Y.; Mohebinia, M.; Wu, X. X.; Tong, T.; Wang, Z. M.; Wu, B.; Zhang, Q.; Ren, Z. F.; Bao, J. M.; Liu, X. F., High ambipolar mobility in cubic boron arsenide revealed by transient reflectivity microscopy. *Science*, **2022**, *377* (6604), 433-436.

[19] Li, S.; Qin, Z.; Wu, H.; Li, M.; Kunz, M.; Alatas, A.; Kavner, A.; Hu, Y., Anomalous thermal transport under high pressure in boron arsenide. *Nature* **2022**, *612* (7940), 459-464.

[20] Choudhry, U.; Pan, F.; He, X.; Shaheen, B.; Kim, T.; Gnabasik, R.; Gamage, G. A.; Sun, H.; Ackerman, A.; Yang, D.-S.; Ren, Z.; Liao, B., Persistent hot carrier diffusion in boron arsenide single crystals imaged by ultrafast electron microscopy. *Matter*, **2023**, *6* (1), 206-216.

[21] Lindsay, L.; Broido, D. A.; Reinecke, T. L., First-principles determination of ultrahigh thermal conductivity of boron arsenide: a competitor for diamond? *Phys. Rev. Lett.*, **2013**, *111* (2), 025901.

[22] Tian, F.; Ren, Z., High Thermal Conductivity in Boron Arsenide: From Prediction to Reality. *Angew. Chem. Int. Ed. Engl.* **2019**, *58* (18), 5824-5831.

[23] Wu, Z. H.; Zhang, Y. X.; Gao, B. X.; Meng, Y.; Shao, H.; Li, D. J.; Xie, P. X.; Wang, W. J.; Li, B. W.; Zhang, C. X.; Shen, Y.; Yin, D.; Chen, D.; Quan, Q.; Yip, S.; Ho, J. C., Synthesis of hexagonal boron arsenide nanosheets for low-power consumption flexible memristors. *Nat. Commun.* **2025**, *16* (1), 4755.

[24] Zhang, J.; Liu, H.; Gao, Y.; Xia, X.; Huang, Z., The sp^2 character of the new two-dimensional AsB with tunable electronic properties predicted by theoretical studies. *Phys. Chem. Chem. Phys.* **2019**, *21* (37), 20981-20987.

[25] Hu, Y.; Li, D.; Yin, Y.; Li, S.; Zhou, H.; Zhang, G., High thermal conductivity driven by the unusual phonon relaxation time platform in 2D monolayer boron arsenide. *RSC Adv*. **2020**, *10* (42), 25305-25310.

[26] Manoharan, K.; Subramanian, V., Exploring multifunctional applications of hexagonal boron arsenide sheet: a DFT study. *ACS Omega*, **2018**, *3* (8), 9533-9543.

[27] Hou, C.; Tai, G. A.; Liu, B.; Wu, Z. H.; Yin, Y. H., Borophene-graphene heterostructure: Preparation and ultrasensitive humidity sensing. *Nano Res.* **2021**, *14* (7), 2337-2344.

[28] Wu, Z. T.; Liang, X. C.; Zhao, Z. L.; Wu, Q. L.; Liu, X.; Liu, Y.; Xu, M. P.; Hou, C.; Tai, G. A., Ultrasensitive and durable borophene-based humidity sensors for advanced human-centric applications. *Chem. Eng. J.* **2024**, 500, 156881.

[29] Li, M. L.; Liu, M.; Qi, F.; Lin, F. R.; Jen, A. K. Y., Self-assembled monolayers for interfacial engineering in solution-processed thin-film electronic devices: design, fabrication, and applications. *Chem. Rev.*, **2024**, *124* (5), 2138-2204.

[30] Choudhry, U.; Pan, F. J.; He, X.; Shaheen, B.; Kim, T.; Gnabasik, R.; Gamage, G. A.; Sun, H. R.; Ackerman, A.; Yang, D. S.; Ren, Z. F.; Liao, B. L., Persistent hot carrier diffusion in boron arsenide single crystals imaged by ultrafast electron microscopy. *Matter*, **2023**, 6 (1), 206-216.

[31] Wang, S. J.; Swingle, S. F.; Ye, H.; Fan, F. R. F.; Cowley, A. H.; Bard, A. J., Synthesis and characterization of a p-type boron arsenide photoelectrode. *J. Am. Chem.Soc.* **2012**, *134* (27), 11056-11059.

[32] Liu, H.; Qin, J. X.; Yang, X. G.; Lv, C. F.; Huang, W. T.; Li, F. K.; Zhang, C.; Wu, Y. R.; Dong, L.; Shan, C. X., Highly sensitive humidity sensors based on hexagonal boron nitride nanosheets for contactless sensing. *Nano Res.* **2023**, *16* (7), 10279-10286.

[33] Pi, C. J.; Chen, W. Q.; Zhou, W.; Yan, S. P.; Liu, Z. C.; Wang, C.; Guo, Q.; Qiu, J. B.; Yu, X.; Liu, B. T.; Xu, X. H., Highly stable humidity sensor based on lead-free $Cs_3Bi_2Br_9$ perovskite for breath monitoring. *J. Mater. Chem. C* **2021**, *9* (34), 11299-11305.

[34] He, J.; Xiao, P.; Shi, J. W.; Liang, Y.; Lu, W.; Chen, Y. S.; Wang, W. Q.; Théato, P.; Kuo, S. W.; Chen, T., High-performance humidity fluctuation sensor for wearable devices via a bioinspired atomic-precise tunable graphene-polymer heterogeneous sensing junction. *Chem. Mater.* **2018**, *30* (13), 4343-4354.

[35] Wu, J.; Sun, Y. M.; Wu, Z. X.; Li, X.; Wang, N.; Tao, K.; Wang, G. P., Carbon Nanocoil-Based Fast-Response and Flexible Humidity Sensor for Multifunctional Applications. *ACS Appl. Mater. Inter.* **2019**, *11* (4), 4242-4251.

[36] Sun, J. Y.; Xiu, K. H.; Wang, Z. Y.; Hu, N.; Zhao, L. B.; Zhu, H.; Kong, F. Z.; Xiao, J. L.; Cheng, L. J.; Bi, X. Y., Multifunctional wearable humidity and pressure sensors based on biocompatible graphene/bacterial cellulose bio aerogel for wireless monitoring and early warning of sleep apnea syndrome. *Nano Energy* **2023**, 108, 108215.

[37] Park, S. Y.; Kim, Y. H.; Lee, S. Y.; Sohn, W.; Lee, J. E.; Kim, D. H.; Shim, Y. S.; Kwon, K. C.; Choi, K. S.; Yoo, H. J.; Suh, J. M.; Ko, M.; Lee, J. H.; Lee, M. J.; Kim, S. Y.; Lee, M. H.; Jang, H. W., Highly selective and sensitive chemoresistive humidity sensors based on rGO/MoS_2 van der Waals composites. *J. Mater. Chem. A* **2018**, *6* (12), 5016-5024.

[38] Iyengar, S. A.; Srikrishnarka, P.; Jana, S. K.; Islam, M. R.; Ahuja, T.; Mohanty, J. S.; Pradeep, T., Surface-Treated Nanofibers as High Current Yielding Breath Humidity Sensors for Wearable

Electronics. *ACS Appl. Electron. Mater.* **2019**, *1* (6), 951-960.

[39] Andric, S.; Tomasevic-Ilic, T.; Boskovic, M. V.; Sarajlic, M.; Vasiljevic-Radovic, D.; Smiljanic, M. M.; Spasenovic, M., Ultrafast humidity sensor based on liquid phase exfoliated graphene. *Nanotechnology* **2021**, *32* (2), 025505.

[40] Alizadeh, T.; Shokri, M., A new humidity sensor based upon graphene quantum dots prepared via carbonization of citric acid. *Sensors and Actuat. B-Chem.* **2019**, *222*, 728-734.

[41] Wu, J.; Wu, Z. X.; Ding, H. J.; Wei, Y. M.; Yang, X.; Li, Z. Y.; Yang, B. R.; Liu, C.; Qiu, L.; Wang, X. T., Multifunctional and high-sensitive sensor capable of detecting humidity, temperature, and flow stimuli using an integrated microheater. *ACS Appl. Mater. Interfaces* **2019**, *11* (46), 43383-43392.

[42] Zhao, Q. N.; Yuan, Z.; Duan, Z. H.; Jiang, Y. D.; Li, X.; Li, Z. M.; Tai, H. L., An ingenious strategy for improving humidity sensing properties of multi-walled carbon nanotubes via poly-L-lysine modification. *Sensors and Actuat. B-Chem.* **2019**, 289, 182-185.

[43] Feng, Y.; Gong, S. J.; Du, E. W.; Yu, K.; Ren, J.; Wang, Z. G.; Zhu, Z. Q., TaS_2 nanosheet-based ultrafast response and flexible humidity sensor for multifunctional applications. *Mater. Chem. C*, **2019**, *7* (30), 9284-9292.

[44] Zhu, K. M.; Tang, Y.; Zhong, X. L.; Xiong, L.; Zhang, Y.; Tan, C. B.; Song, H. J.; Wang, J. B., Improved response/recovery time and sensitivity of SnSe nanosheet humidity sensor by LiCl incorporation. *Adv. Electron. Mater.* **2020**, *6* (5), 1901330.

[45] Liang, Y. N.; Ding, Q. L.; Wang, H.; Wu, Z. X.; Li, J. Y.; Li, Z. Y.; Tao, K.; Gui, X. C.; Wu, J., Humidity sensing of stretchable and transparent hydrogel films for wireless respiration monitoring. *Nano-Micro Lett.* **2022**, *14* (1), 183.

[46] Zhao, R. R.; Luo, J. X.; Ke, T.; Zhang, J. W.; Astruc, D.; Zhou, J.; Gu, H. B., Ultra-tough, highly stable and self-adhesive goatskin-based intelligent multi-functional organogel e-skin as temperature, humidity, strain, and bioelectric four-mode sensors for health monitoring. *Chem. Eng. J.* **2024**, 485, 149816.

[47] Chen, X. Y.; Kong, L. W.; Mehrez, J. A. A.; Fan, C.; Quan, W. J.; Zhang, Y. W.; Zeng, M.; Yang, J. H.; Hu, N. T.; Su, Y. J.; Wei, H.; Yang, Z., Outstanding humidity chemiresistors based on imine-linked covalent organic framework films for human respiration monitoring. *Nano-Micro Lett.* **2023**, *15* (1), 149.

[48] Wang, N.; Tong, J. H.; Wang, J. J.; Wang, Q.; Chen, S. B.; Sheng, B., Polyimide-sputtered and polymerized films with ultrahigh moisture sensitivity for respiratory monitoring and contactless sensing. *ACS Appl. Mater. Interfaces*, **2022**, *14* (9), 11842-11853.

[49] Agmon, N., The Grotthuss Mechanism. *Chem. Phys. Lett.* **1995**, *244* (5-6), 456-462.

[50] Mangiatordi, G. F.; Butera, V.; Russo, N.; Laage, D.; Adamo, C., Charge transport in poly-imidazole membranes: a fresh appraisal of the Grotthuss mechanism. *Phys. Chem. Chem. Phys.* **2012**, *14* (31), 10910-10918.

Electronic Supplementary Material

Self-powered flexible humidity sensors based on amorphous boron arsenide nanosheets

Zenghui Wu[1], Yuxuan Zhang[1], Boxiang Gao[1], Dongchang He[1], Yan Yan[1], You Meng[1], He Shao[1], Bowen Li[1,2], Weijun Wang[1], Dengji Li[1], Pengshan Xie[1], Dylan Xianyu Fan[3], SenPo Yip[4], and Johnny C. Ho[1,2,4,5] ✉

[1] *Department of Materials Science and Engineering, City University of Hong Kong, Hong Kong 999077, China*
[2] *Shenzhen Research Institute, City University of Hong Kong, Shenzhen 518057, China*
[3] *American International School, Hong Kong 999077, China*
[4] *Institute for Materials Chemistry and Engineering, Kyushu University, Fukuoka 816-8580, Japan*
[5] *State Key Laboratory of Terahertz and Millimeter Waves, City University of Hong Kong, Hong Kong 999077, China*

✉ Address correspondence to johnnyho@cityu.edu.hk

Supporting information to https://doi.org/10.26599/NR.2026.94908321

Experimental Section

Material synthesis: All the chemicals, including arsenic (As, ≥99.999%), sodium borohydride ($NaBH_4$, 99%), and hydrochloric acid (HCl, 37%), were purchased from Sigma-Aldrich and used without further processing. Ultrapure deionized (DI) water was used for all solution preparations. Sodium borohydride and arsenic were mixed in a molar ratio of 1:2 and ground in an agate mortar for half an hour in a glove box. Then, 250 mg was placed in a quartz boat and reacted in a tubular furnace in a low-pressure hydrogen atmosphere. The *a*-BAs were prepared by an in-situ chemical reaction of sodium borohydride with elemental arsenic at 600 ℃ for 60 min. After the reaction, the powder was soaked in 5% hydrochloric acid for 10 min, ultrasonicated in deionized water for 30 min, and then centrifuged to remove the upper dispersion. The precipitate obtained by centrifugation was washed with deionized water and then with alcohol, followed by three additional centrifugations to obtain amorphous boron arsenide nanosheets.

Material characterization: SEM images were obtained with the FEI Quanta 450 FESEM analysis system. Atomic force microscopy (AFM, Bruker Multimode 8 Nanoscope) was used to get the thickness profile of the as-synthesized *a*-BAs nanosheets. Transmission electron microscopy (TEM) images and selected area electron diffraction (SAED) patterns were obtained using an FEI Talos F200S field-emission transmission electron microscope at an accelerating voltage of 200 kV. Energy dispersive X-ray spectroscopy mappings were carried out on a Thermo Fisher Scientific Spectra 300 S/TEM at an accelerating voltage of 300 kV. Chemical states and elemental composition analyses were performed using X-ray photoelectron spectroscopy (ESCALAB 250Xi, Thermo Fisher Scientific Inc.) with a focused, monochromatized Al Kα irradiation. XRD patterns were collected on a Rigaku SmartLab high-resolution X-ray diffractometer. Raman measurement was carried out on a WITec alpha300 R Raman System with a laser wavelength of 532 nm. Attenuated total reflectance Fourier transform infrared (ATR-FTIR) spectroscopy was recorded on a PerkinElmer FTIR Spectrometer. At room temperature, UV-vis absorption spectra were recorded on a Hitachi UH4150 UV-VIS-NIR Spectrophotometer.

Device fabrication and measurement: The BAs powders (1 mg) were dispersed uniformly in 1 mL of alcohol. Then, the dispersion was drop-coated onto PI substrates and dried in air. The corresponding Au interdigital electrode (thickness = 40 nm, width = 0.2 mm, and length = 10 mm) was deposited by evaporation. A source measurement unit system (Agilent 4155C semiconductor analyzer) was used to measure the device's current at an applied voltage of 0 or 1 V at room temperature.

DFT calculation： The Ab initio calculations were performed within the DFT framework with the Vienna Ab-initio Simulation Package (VASP) [1, 2]. The electron-electron exchange-correlation energy was approximated by the generalized gradient approximation (GGA) with the Perdew-Burke-Ernzerhof (PBE) functional [3]. Projected augmented wave potentials were used to describe core-level electron wave functions. The amorphous BAs were modeled by a melt-quench-relaxation method in a supercell that contains 57 B atoms and 56 As atoms based on the atomic ratio from EDS analysis. In detail, the initial atomic positions were randomized by melting at 3000 K for 10 ps and then quenched from 1500 to 300 K with a cooling rate of -100 K ps^{-1}. The model was further relaxed until the atomic forces were less than 10^{-2} eV $Å^{-1}$. The cutoff energy of 450 eV and the convergence criterion for the self-consistent calculation of 10^{-4} eV were used. For Brillouin zone sampling, the Γ point was used for ab initio dynamic calculations, and a 3 × 3 × 3 grid mesh was employed for electronic structure calculations. The differential charge density was derived by subtracting the BAs and gas molecule charge density from the post-adsorption charge density.

[1] Kresse, G.; Furthmuller, J., Efficient iterative schemes for ab initio total-energy calculations using a plane-wave basis set. *Phys. Rev. B*, **1996**, *54* (16), 11169-11186.
[2] Perdew, J. P.; Burke, K.; Ernzerhof, M., Generalized gradient approximation made simple. *Phys. Rev. Lett.* **1996**, *77* (18), 3865-3868.
[3] Kresse, G.; Joubert, D., From ultrasoft pseudopotentials to the projector augmented-wave method. *Phys. Rev. B*, **1999**, *59* (3), 1758-1775.

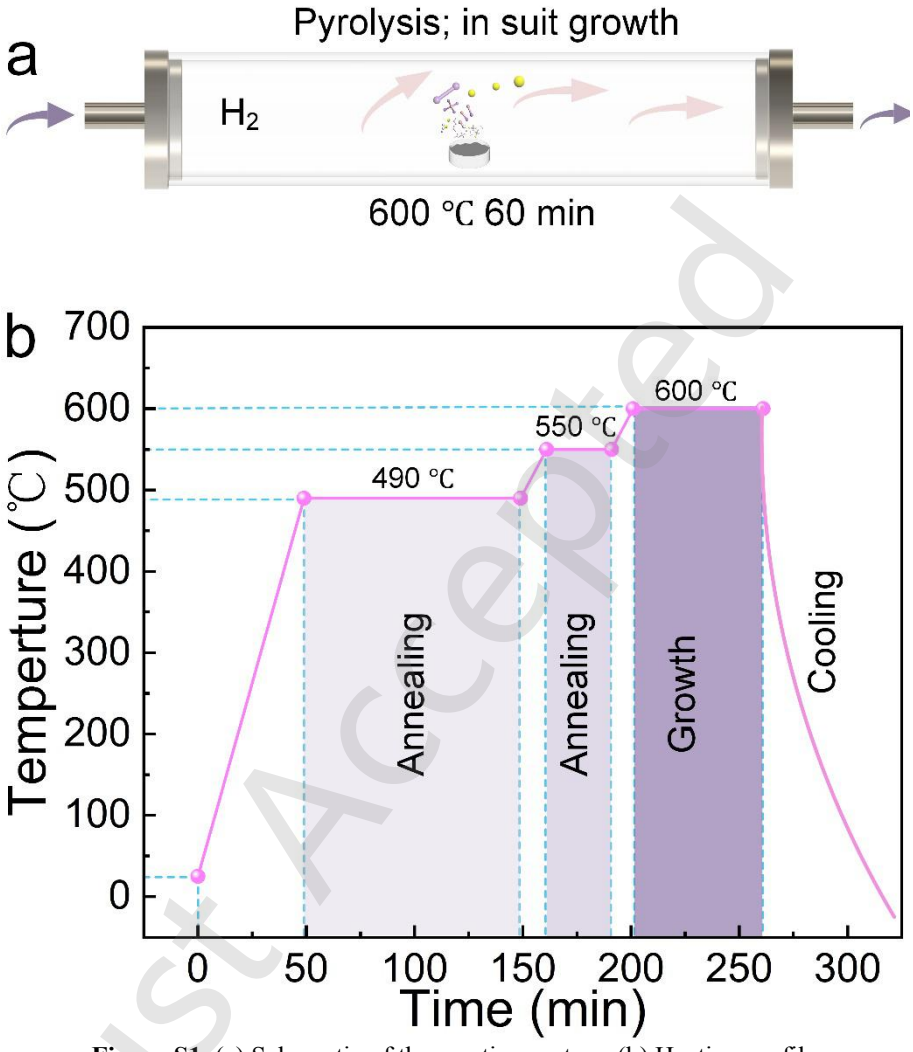

Figure S1. (a) Schematic of the reaction system. (b) Heating profile.

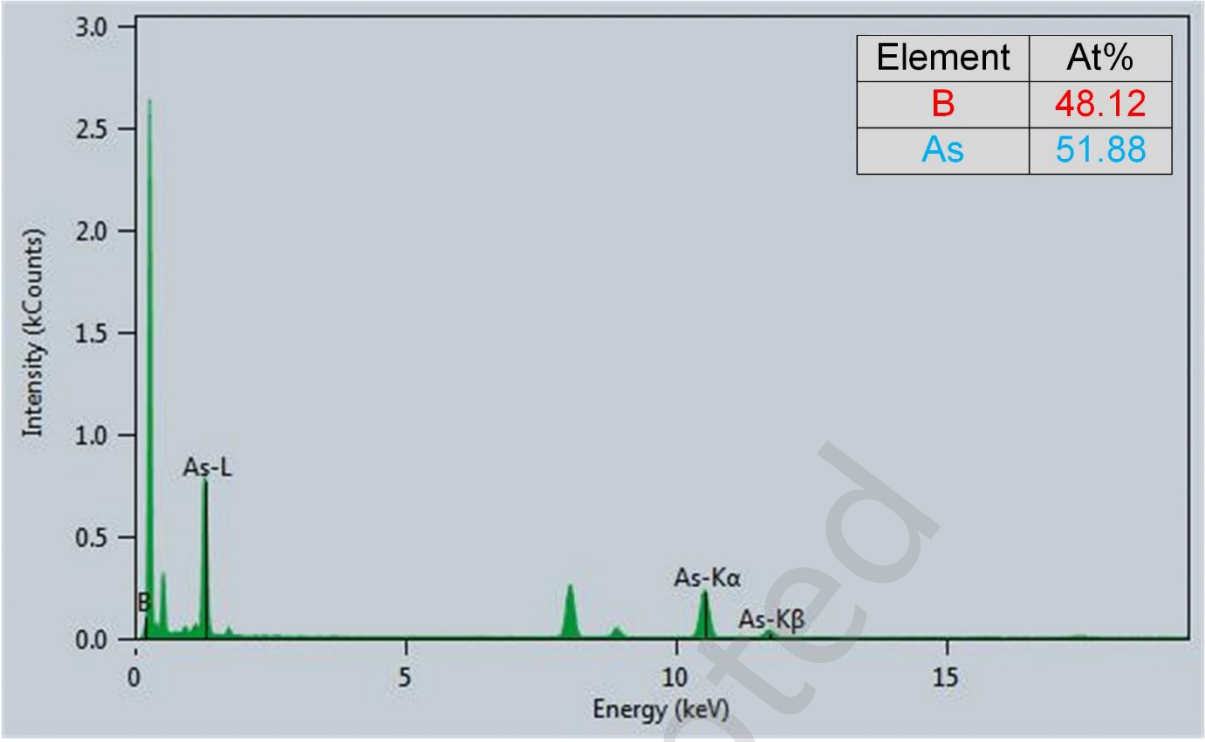

Figure S2. Typical EDS spectra of the *a*-BAs nanosheets.

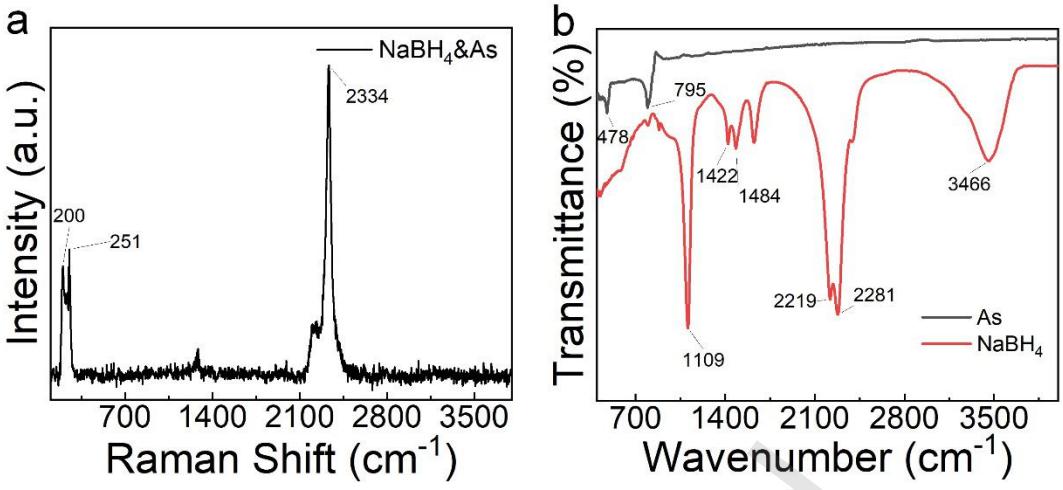

Figure S3. (a) Raman and (b) IR spectrum of the source.

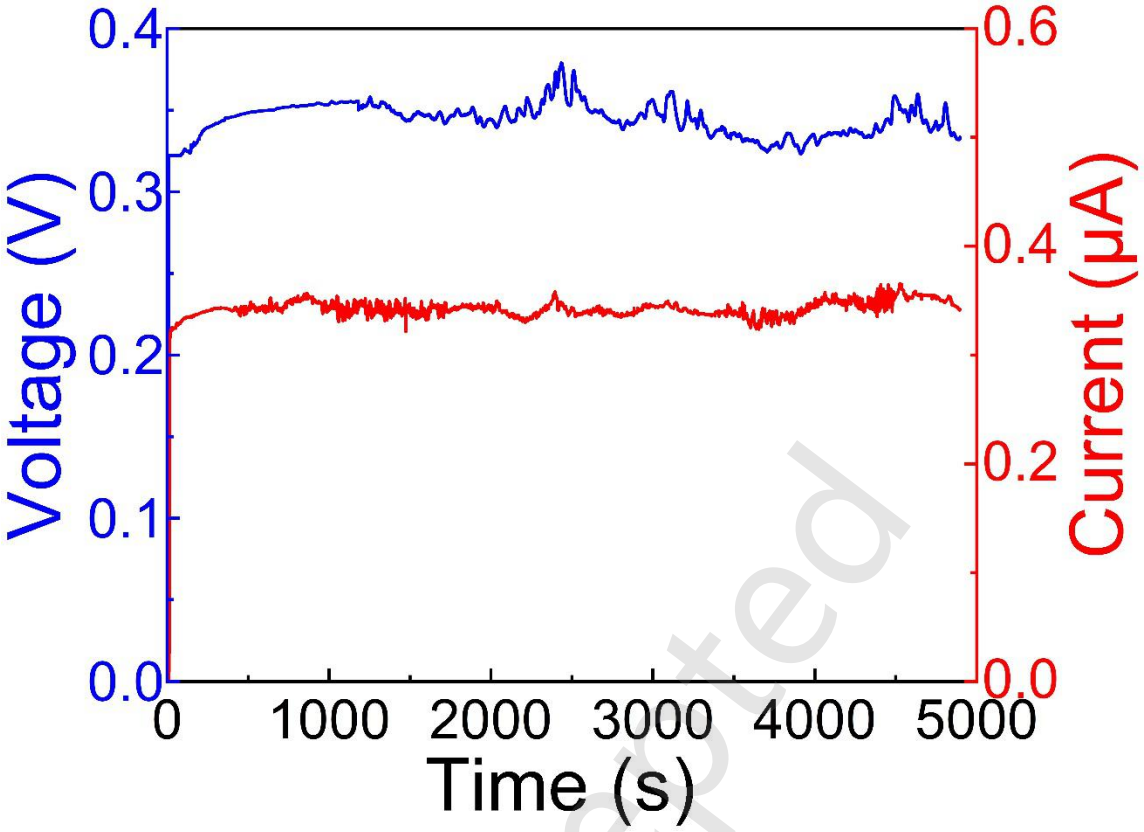

Figure S4. Sustainable voltage and current output of the BAs-based device to 85% RH at room temperature.

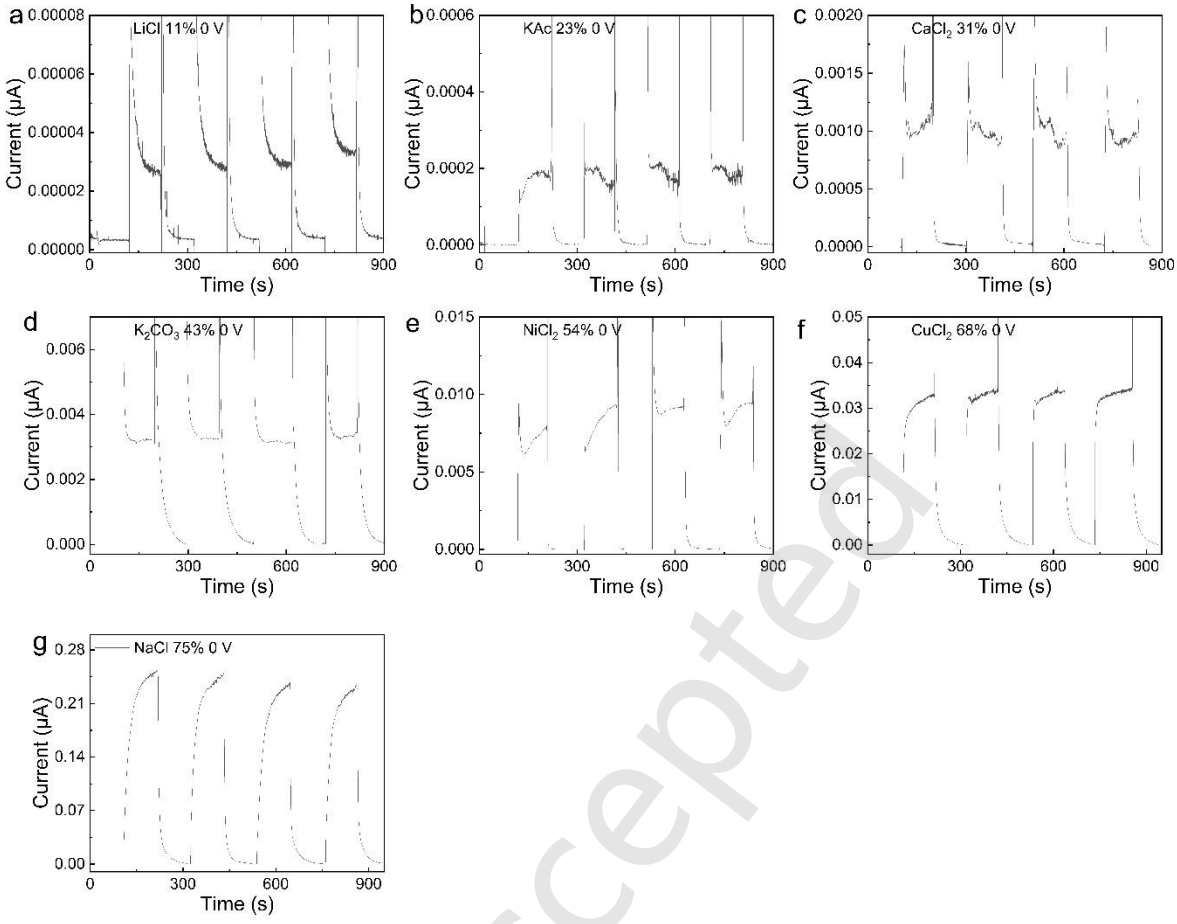

Figure S5. Cyclic performance of the boron arsenide sensor under 0 V bias at (a) 11% RH, (b) 23% RH, (c) 31% RH, (d) 43% RH, (e) 54% RH, (f) 68% RH, and (g) 75% RH, respectively.

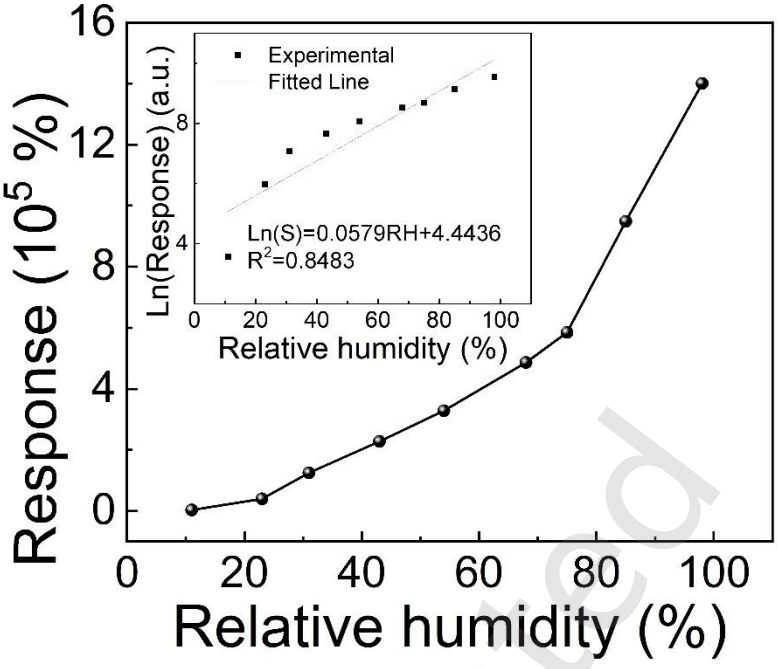

Figure S6. Response of the sensor in the range of 11% to 97% RH.

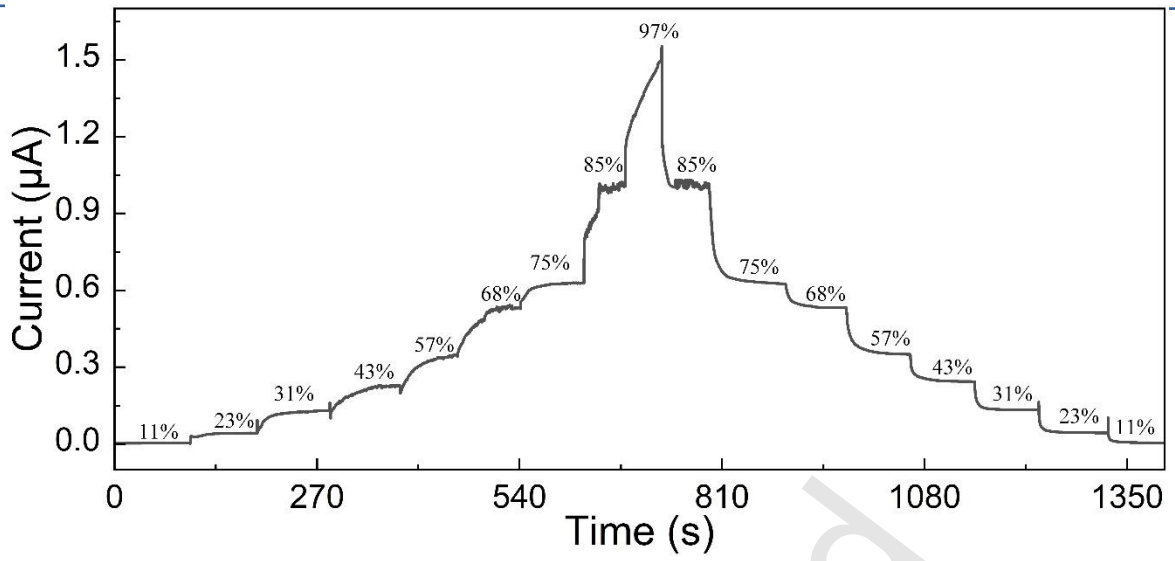

Figure S7. Current curves of the humidity sensor during the adsorption and desorption processes of water molecules.

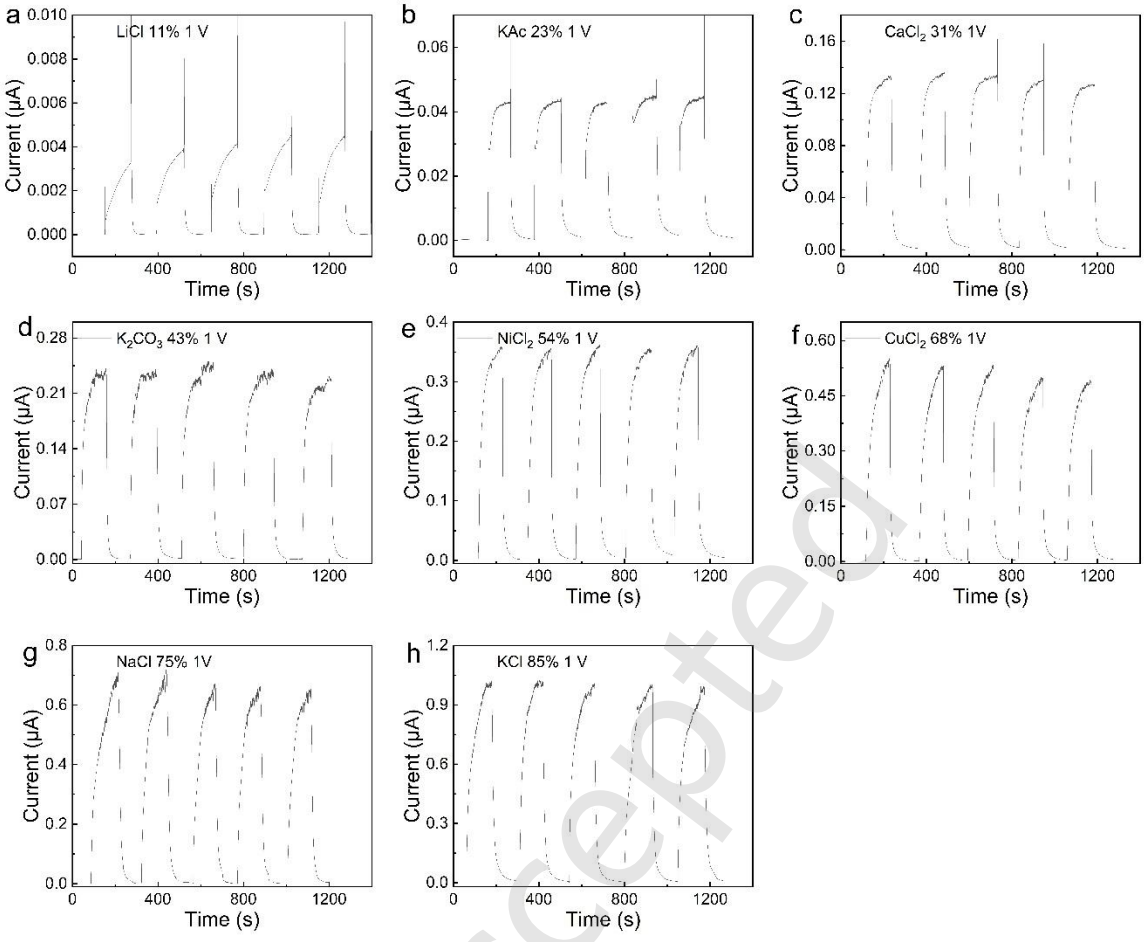

Figure S8. Cyclic performance of the boron arsenide sensor under 1 V bias at (a) 11% RH, (b) 23% RH, (c) 31% RH, (d) 43% RH, (e) 54% RH, (f) 68% RH, (e) 75% RH and (f) 85% RH, respectively.

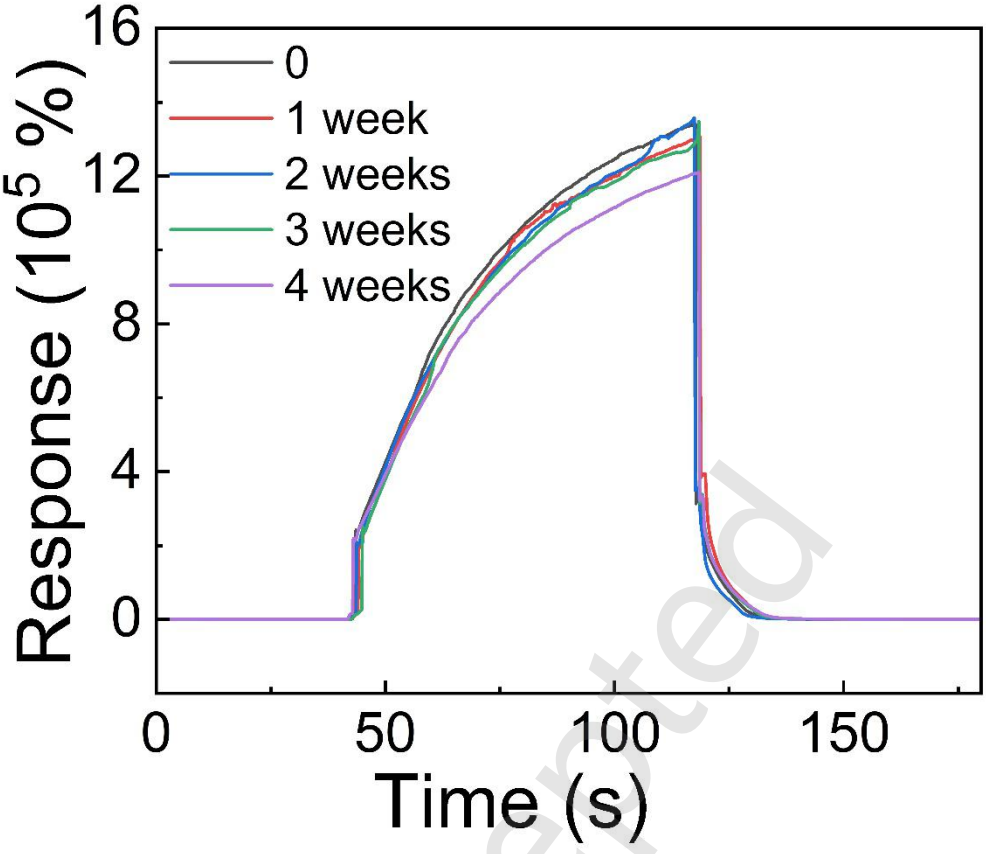

Figure S9. Long-term stability of the sensor with 1 V at 97% RH.

Table S1 Comparison of recently reported humidity sensors

Structure & Materials	Response (%)	Response/ Recovery time (s)	Measured RH value (%)	Humidity range	Ref.
GNCP	2.84×10^4	0.02/0.017	97.00	0-97% RH	[34]
Carbon nanocoils	12.20	1.9/1.5	80.00	4-95% RH	[35]
Bacterial cellulose and graphene hybrids	3.00×10^4	187/41	95.00	11-95% RH	[36]
r-GO/MoS_2	2.49×10^3	6.3/30.8	85.00	5-95% RH	[37]
PVDF/rGO/ PANi based nanofibers	60.00	1	95.00	0-95% RH	[38]
Graphene	1.10×10^2	0.028/0.03	88.00	8-95% RH	[39]
GQDs	1.13×10^3	10	97.00	0-97% RH	[40]
GO	5.31×10^3	3/7.7	95.00	8-95% RH	[41]
MWCNTs	6.60×10^2	30	91.50	0-91.5% RH	[42]
α′-4H borophene	1.50×10^2	2.3/0.7	85.00	67-85% RH	[27]
Borophene–graphene	4.20×10^3	10.5/8.3	85.00	0-85% RH	[27]
Borophene–MoS_2	1.55×10^4	2.5/3.1	97.00	0-97% RH	[9]
Borophene-BC_2N	2.20×10^4	11.82/1.41	97.00	11-97% RH	[10]
Borophene glass	1.83×10^5	28.8/2.6	97.00	11-97% RH	[28]
h-BN nanosheets	2.84×10^4	3/5.5	85.00	11-85% RH	[32]
$Cs_3Bi_2Br_9$	9.87×10^2	5.56/6.24	90.00	0-90% RH	[33]
h-WO_3	3.10×10^4	1.5/15.2	95.00	11-95% RH	[6]
WSe_2	0.42	40/30	90.00	40-90% RH	[13]
Bi_2O_2S	2.58×10^3	0.4/2.4	90.00	10-90% RH	[14]
MoS_2 nanosheets	4.34×10^2	30/40	96.00	11-96% RH	[15]
TaS_2 nanosheets	2.02×10^2	0.6/2	95.00	11-95% RH	[43]
SnSe nanosheet	1.40×10^4	22/7	95.00	0-95% RH	[44]
PAM/Tapioca	1.35×10^4	276/227	98.00	11-98% RH	[45]
PMATG	2.06×10^3	132/150	97.00	24.2-97% RH	[46]
$COF_{TAPB\text{-}DHTA}$ Film	3.90×10^4	0.4/1	98.00	13-98% RH	[47]
Polyimide	6.00×10^3	2.4/1.2	95.00	11-95% RH	[48]
a-BAs	8.40×10^6	37.6/19.6	85.00	0-85% RH	This work (0 V)
a-BAs	1.400×10^6	44.9/7.2	97.00	0-97% RH	This work (1 V)